Nano Research 2016, 9(12): 3632–3643
DOI 10.1007/s12274-016-1233-4
Research Article
ISSN 1998-0124
CN 11-5974/O4

A wrinkle to sub-100 nm yolk/shell Fe_3O_4@SiO_2 nanoparticles

Hualin Ding[1], Yunxia Zhang[1], Sichao Xu[1], and Guanghai Li[1,2] (✉)

[1] *Key Laboratory of Material Physics, Anhui Key Laboratory of Nanomaterials and Nanotechnology, Institute of Solid State Physics, Chinese Academy of Sciences, Hefei 230031, China*
[2] *School of Chemistry and Materials Science, University of Science and Technology of China, Hefei 230026, China*

Received: 12 April 2016
Revised: 27 July 2016
Accepted: 28 July 2016

KEYWORDS
nanostructures,
silica self-template,
selective acidic etching,
yolk/shell

ABSTRACT

Yolk/shell nanoparticles (NPs), which integrate functional cores (likes Fe_3O_4) and an inert SiO_2 shell, are very important for applications in fields such as biomedicine and catalysis. An acidic medium is an excellent etchant to achieve hollow SiO_2 but harmful to most functional cores. Reported here is a method for preparing sub-100 nm yolk/shell Fe_3O_4@SiO_2 NPs by a mild acidic etching strategy. Our results demonstrate that establishment of a dissolution–diffusion equilibrium of silica is essential for achieving yolk/shell Fe_3O_4@SiO_2 NPs. A uniform increase in the silica compactness from the inside to the outside and an appropriate pH value of the etchant are the main factors controlling the thickness and cavity of the SiO_2 shell. Under our "standard etching code", the acid-sensitive Fe_3O_4 core can be perfectly preserved and the SiO_2 shell can be selectively etched away. The mechanism of regulation of SiO_2 etching and acidic etching was investigated.

1 Introduction

Yolk/shell nanostructures, which integrate the porous shell, functional cores, and the hollow cavity between them, are promising multifunctional materials [1–5]. Compared to core/shell nanostructures, the unique properties of yolk/shell nanostructures, such as low density, excellent loading capacity, a confined environment, large surface area, moveable cores, and high permeability, have many potential applications such as bioactive molecular carriers in biomedicines [6–9], as confined-space catalysts in nanoreactors [10–13], and as lithium-ion batteries in energy storage [14–16]. Silica, carbon, polymer, metals, and oxides are typical shell materials in well-known yolk/shell nanostructures. The silica shell has drawn much attention because of its optical transparency, biocompatibility, and easily achievable surface modification, besides the unique properties mentioned above [17–19].

Different methods have been explored to engineer functional yolk/silica shell nanostructures [20, 21]. Soft template and hard template methods are two commonly used strategies for creating hollow cavities [22–26]. The former is relatively simple; it employs a

Address correspondence to ghli@issp.ac.cn

micelle or vesicle as the template, but it is difficult to control the hollow cavity volume and the size and uniformity of the yolk/shell nanoparticles (NPs). The latter method can form a highly uniform cavity size, yet the process is generally tedious, complex, and uneconomical because of the use of a sacrificial template. In contrast, the selective etching method based on the structural difference in the silica shell is promising, with a relatively simple process because of the absence of any surface primer [27, 28]. Nevertheless, the preparation of the yolk silica–shell structure is still a multistep process, comprising the formation of two structurally different silica layers and the removal of the middle layer. For practical applications, the development of a simple, economical, and scalable self-template strategy that can effectively create a hollow cavity between the functional core and the silica shell is very important.

A "surface protected etching" strategy based on a silica self-template has been devised and successfully used to prepare yolk/silica shell NPs [29, 30]. Since the etching is conducted in a strong alkaline solution, it is difficult to control the etching rate; therefore, this strategy is unsuitable for preparing sub-100 nm diameter silica shells. The yolk/shell nanostructures with sub-100 nm diameters are indispensable for *in vivo* applications to elude the uptake by the reticuloendothelial system (RES) [31]. Although significant progress has been made on the preparation of sub-100 nm yolk/silica shell NPs, a template and a protective agent are still needed [8, 32, 33]. There are some reports on the selective etching of yolk/shell nanostructures with sub-100 nm diameter silica shells based on the silica self-template strategy [34–36]. Since the recondensation reaction of Si–OH groups generated from the dissolution of the silica network always occurs, the presence of impurities or even structural change in the silica shell is inevitable [35], resulting in a deterioration of the stability and repeatability of the etching process. The selective acidic etching based on the silica self-template is a promising route for solving these problems, as has been proved in the preparation of multilayer silica spheres by utilizing hydrofluoric acid (HF) [28] and hollow silica spheres using generic acids (HCl or H_2SO_4) [37]. Nevertheless, acidic etching of only silica spheres larger than 100 nm and without a functional core has been reported. Functional cores like Fe_3O_4 are acid sensitive and can be readily dissolved in the HCl solution [9, 38, 39]. Thus, it is generally considered that an acidic etchant is not feasible for transforming the core/shell Fe_3O_4@SiO_2 NPs into the yolk/shell Fe_3O_4@SiO_2 NPs, thereby preserving the Fe_3O_4 core.

Here, we demonstrate a strategy for the preparation of yolk/shell Fe_3O_4@SiO_2 NPs by selective acidic etching of the core/shell Fe_3O_4@SiO_2 NPs with a single structural shell in a generic acidic solution (CH_3COOH or HCl). The kinetics-controlled etching protocol in modulating the cavity size and shell thickness was investigated, the acidic etching mechanism is discussed, and a "standard etching code" is proposed.

2 Experimental

2.1 Chemicals

Analytical grade ethanol, hexane, cyclohexane, aqueous ammonia (25%–28%), tetraethyl orthosilicate (TEOS, 98%), CH_3COOH (≥99.5%), HCl (36%–38%), polyvinylpyrrolidone (PVP 10, M_W ~ 10,000), sodium hydroxide, and iron (III) chloride hexahydrate (99.99%) were obtained from Sinopharm Chemical Reagent Co. Ltd. (Shanghai). 1-Octadecene (tech. 90%) and polyoxyethylene (5) nonylphenylether (Igepal CO-520) were purchased from Aldrich. Oleic acid (90%) was obtained from Alfa Aesar. All the chemicals were used as received without further purification. The water used was purified through a Millipore system.

2.2 Synthesis

2.2.1 Fe_3O_4@SiO_2 NPs

Fe_3O_4 NPs were prepared by the thermal decomposition method as reported previously [40] and the silica coating was prepared via a reverse microemulsion method [41]. For a typical process, 0.5 g Igepal CO-520 was dispersed in 11 mL cyclohexane and sonicated for 10 min. Then, 0.5 mL of Fe_3O_4 solution (about 13.1 nm size, 2.5 mg/mL in cyclohexane), i.e., 1.25 mg Fe_3O_4, was added to the above solution with continuous stirring. Subsequently, 0.2 mL of ammonium hydroxide (25%–28%) was added to the above solution mixture.

Finally, 0.21 mL of TEOS was added by the equivalently fractionated drop method (adding 35 μL per 16 h). The resulting Fe_3O_4@SiO_2 core–shell NPs were collected after centrifuging and washing, and redispersed in deionized water. Based on the amount of TEOS used, SiO_2 shells ranging from about 11.1 to 22.6 nm in thickness can be formed.

2.2.2 *Additional layer of SiO_2 shell on Fe_3O_4@SiO_2 NPs by Stöber method*

The Fe_3O_4@SiO_2 NPs prepared using the above method were added to a mixture of ethanol (9 mL), water (1.7 mL), and ammonia (0.3 mL), and stirred for 1 h at room temperature. Then, 50 μL of TEOS was added dropwise, and the reaction proceeded for 6 h. The products were collected after centrifuging and washing several times with ethanol, and redispersed in de-ionized water.

2.2.3 *SiO_2 NPs*

According to a typical reverse microemulsion method, 0.5 g Igepal CO-520 was dispersed in 11 mL cyclohexane and sonicated for 10 min. Subsequently, 0.2 mL of ammonium hydroxide (25%–28%) was added to the above solution mixture. Finally, 0.28 mL of TEOS was added by the equivalently fractionated drop method (adding 35 μL per 16 h). The resulting SiO_2 NPs were collected after centrifuging and washing, and redispersed in de-ionized water.

2.2.4 *Yolk/shell Fe_3O_4@SiO_2 NPs*

Briefly, 16 mg of the as-prepared Fe_3O_4@SiO_2 NPs were dispersed in de-ionized water (10 mL) by ultrasonication, and then, the pH value of the solution was adjusted to 3.9 by addition of acetic acid. Finally, the reaction was kept at 160 ℃ for 24 h under continuous stirring (denoted as "standard etching code"). The resultant product was separated by centrifuging, followed by washing alternately with de-ionized water and ethanol 2 times.

2.2.5 *Hollow SiO_2 NPs*

As-prepared SiO_2 NPs in 10 mL de-ionized water were etched using the "standard-etching code". The resultant product was separated by centrifuging, followed by washing alternately with de-ionized water and ethanol 2 times.

2.3 Characterization

Transmission electron microscopy (TEM) images were obtained using a JEOL 2010 operated at an accelerating voltage of 200 kV. Inductively coupled plasma-atomic emission spectrometry (ICP-AES, ICP6300, Thermo Fisher Scientific) was used to evaluate the Si content of the dissolved SiO_2 in the reaction solution. Inductively coupled plasma-mass spectrometry (ICP-MS, iCAP Qc, Thermo Fisher Scientific) was utilized to determine the Fe content of the dissolved Fe_3O_4 in the etching solution. To avoid the influence of yolk/shell Fe_3O_4@SiO_2 NPs on the determination of the dissolved Fe and Si content in the reaction solution in the ICP measurements, the supernatant was isolated by centrifuging several times. The field-dependent magnetization measurement was performed on a superconducting quantum interference device (SQUID) at room temperature.

3 Results and discussion

Figure 1(a) shows a typical TEM image of the core/shell Fe_3O_4@SiO_2 NPs prepared by thermal decomposition combined with the reverse microemulsion method. The core/shell Fe_3O_4@SiO_2 NPs are highly monodispersed with a ~13.1-nm-thick Fe_3O_4 single-core and ~18.1-nm-thick SiO_2 shell. The core/shell Fe_3O_4@SiO_2 NPs can be converted into the yolk/shell Fe_3O_4@SiO_2 NPs by a mild acidic etching approach using our "standard etching code" described in the Experimental section, as shown in Fig. 1(b). The inner part of the SiO_2 shell is selectively etched away, leaving a vast cavity between the Fe_3O_4 core and the SiO_2 shell. Interestingly, the size of the Fe_3O_4 core and the diameter of the SiO_2 shell in the yolk/shell Fe_3O_4@SiO_2 NPs are nearly the same as those in the core/shell Fe_3O_4@SiO_2 NPs, and the SiO_2 shell is smooth. Because no surface protective agent was used, the preservation of the smooth outer SiO_2 surface in the yolk/shell Fe_3O_4@SiO_2 NPs indicates that the etching process takes place only in the inner part of the SiO_2 shell. Significantly, no change was observed in the size of the Fe_3O_4 core after etching, suggesting the effectiveness of the gentle acidic etchant. The thickness of the retained SiO_2 shell

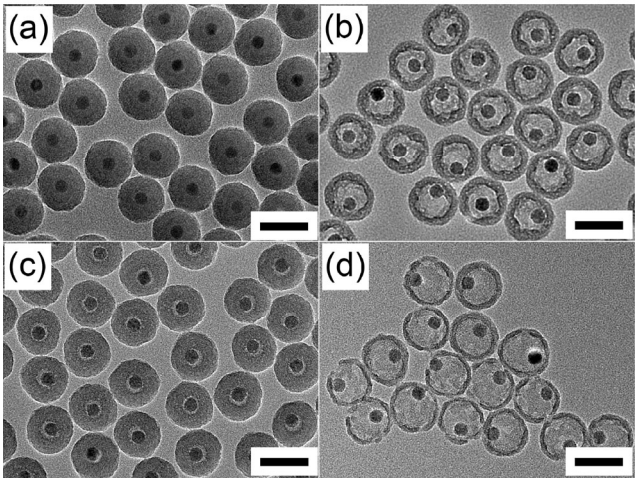

Figure 1 TEM images of (a) core/shell Fe_3O_4@SiO_2 NPs with a Fe_3O_4 core of 13.1 nm and SiO_2 shell thickness of 18.1 nm, and yolk/shell Fe_3O_4@SiO_2 NPs with the remaining SiO_2 shell of thickness (b) 8.3, (c) 16.0, and (d) 4.4 nm. Scale bar = 50 nm.

(the size of the cavity) can be tuned from about 18.1 to 4.4 nm (from 0 to 13.7 nm) by using different etching parameters (see Figs. 1(c) and 1(d), which will be discussed in detail later). Our selective etching method can also be used to prepare yolk/shell Fe_3O_4@SiO_2 NPs from core/shell Fe_3O_4@SiO_2 NPs with different sizes, as shown in Fig. 2. It was found that the acid etching method is also suitable for the Stöber silica NPs, as shown in Fig. S1 in the Electronic Supplementary Material (ESM).

There are four key factors for achieving a perfect transformation from core/shell Fe_3O_4@SiO_2 NPs to yolk/shell Fe_3O_4@SiO_2 NPs by our acidic etching method. First, the degree of condensation of the inner SiO_2 shell should be lower than that of the outer SiO_2 shell. Second, there are some pores present on the SiO_2 shell, so that the etching species can penetrate the inner space of the SiO_2 shell. Third, the etchants must be insensitive to the Fe_3O_4 core. Lastly, the reformation of the Si–O–Si bonds is weak or can be effectively depressed to ensure repeatability and structural stability of the remaining SiO_2 shell after etching.

The SiO_2 shell in the core/shell Fe_3O_4@SiO_2 NPs is obtained by the reverse microemulsion method. During the initial stage of the SiO_2 coating, the hydrolysis of TEOS is much faster than the condensation of the Si–OH groups, resulting in a rapid formation of the silica network (Si–O–Si) with partial Si–OH groups [42, 43]. Then, the TEOS hydrolysis rate will drop exponentially with time, leaving enough time for the condensation of the Si–OH groups. In contrast, the electronic density of the Si atoms decreases with increasing degree of condensation in the order Si–OH > Si–O–Si [44], facilitating the condensation reaction of the Si–OH groups and the formation of a compact silica network. Thus, the hardness of the SiO_2 shell increases gradually from the inside to the outside. This result indicates that the compositional inhomogeneity is crucial for the formation of the cavity, as has been proved in a previous study [36], in which the compositional inhomogeneity is formed by the difference

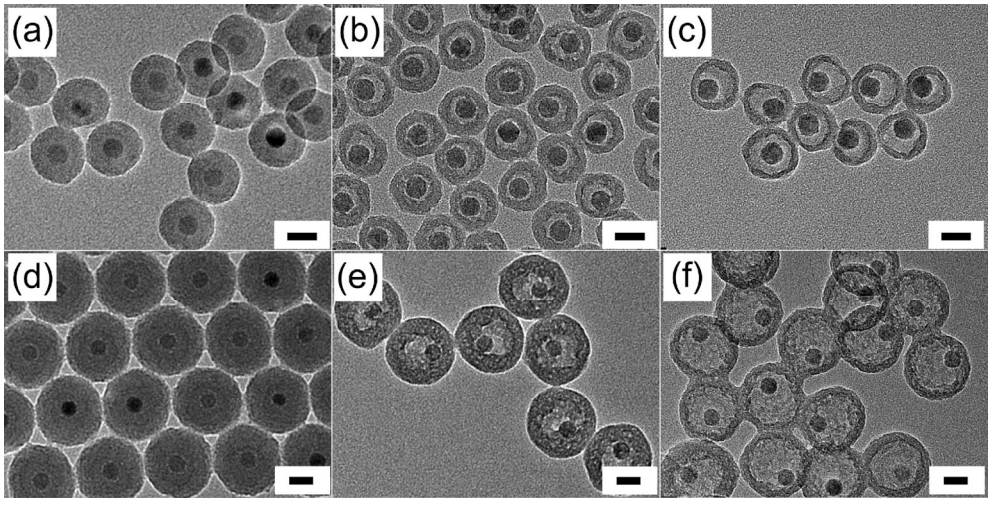

Figure 2 TEM images of core/shell Fe_3O_4@SiO_2 NPs with a shell thickness of (a) 11.1 and (d) 22.6 nm, and the corresponding yolk/shell Fe_3O_4@SiO_2 NPs with the remaining SiO_2 shell of thickness (b) 7.9, (c) 4.7, (e) 13.8, and (f) 4.7 nm. Scale bar = 20 nm.

in the ion-paired polyelectrolytes in the formation process of silica.

The etching temperature used in our "standard etching code" is 160 ℃, and is much higher than the 95 ℃ reported in literature [34, 45, 46]. The synthesis rate of the SiO_2 is comparatively slow in this study, resulting in a relatively hard shell. As a result, a high etching temperature is employed because more energy is needed to break the Si–O–Si bond (Fig. 3). In a separate experiment, an additional SiO_2 layer was coated on the outer surface of the preformed core/shell Fe_3O_4@SiO_2 NPs by the Stöber method, and were etched using our "standard etching code." It was found that both the SiO_2 layer prepared by the Stöber method and the inner SiO_2 layer formed by the reverse microemulsion method were almost etched away, leaving only the middle SiO_2 layer prepared by the reverse microemulsion method (Fig. S2 in the ESM). This result demonstrates that the exterior SiO_2 layer prepared by the reverse microemulsion method is harder than that prepared by the Stöber protocol.

The solubility of silica depends on the degree of polymerization of the SiO_2 shell. The degree of crosslinking is different from the inside to the outside of the SiO_2 shell prepared by the reverse microemulsion method, and thus, the condensation degree of the SiO_2 shell is crucial in controlling the size and uniformity of the cavity, as well as the integrity and solidity of the final SiO_2 shell. A uniform gradient of the degree of condensation in the radial direction of the SiO_2 shell is favorable for achieving a homogeneous cavity and shell thickness. Using a suitable etchant, the interior SiO_2 layer with a lesser degree of condensation will be etched out, leaving the exterior SiO_2 layer, which has a high degree of condensation.

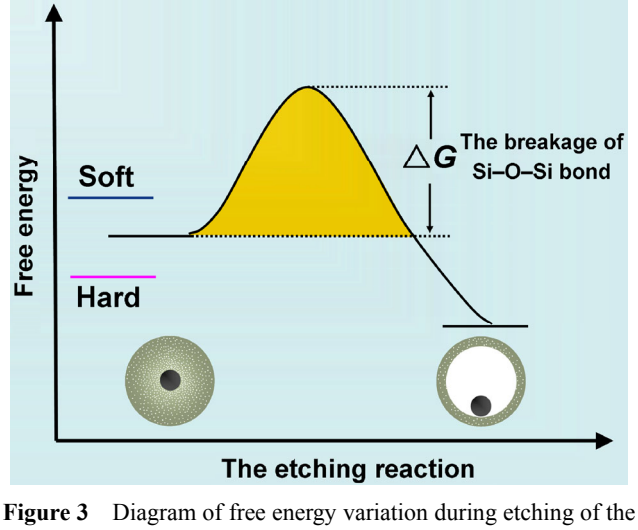

Figure 3 Diagram of free energy variation during etching of the SiO_2 shell.

The SiO_2 shell prepared by the reverse microemulsion method already contains massive nanopores (Fig. S3 in the ESM) [47], and these pores are beneficial for the penetration of the etchant into the inner part of the SiO_2 shell. On the other hand, these nanopores will also serve as diffusion channels for the dissolved silica species. It was found that the innermost part of the SiO_2 shell can be etched away, leaving a cavity within 2 h, as shown in Fig. S4 in the ESM. In a previous study, pre-soaking in an acidic solution for 24 h was needed for forming a cavity inside the SiO_2 spheres [37]. This result indicates that the nanopores in the SiO_2 shell formed by the present method are efficient in transporting both the etchant and the dissolved silica species because of a short diffusion distance of the small silica particles (<100 nm).

The pH value of the etchant is another key factor. The etching of the SiO_2 shell depends on the breakage of the Si–O–Si bond. On the other hand, the Si–O–Si bond will easily reform in alkaline solution, which is harmful for maintaining a stable SiO_2 shell and a repeatable etching process. If etching occurs in a weak alkaline solution, no visible cavity is produced except for some nanopores in the interior of the SiO_2 shell for the core/shell Fe_3O_4@SiO_2 NPs with a size less than 100 nm. In addition, the outer surface of the SiO_2 shell became rough and irregular (Fig. 4), implying that breakage and reformation of the Si–O–Si bond takes place on the SiO_2 shell. In fact, reformation of the Si–O–Si bonds still occurs even when etching in an acidic medium with pH values over the 5–7 range (Figs. S5(a) and S5(b) in the ESM) or in a pure water system (pH = 8.1, see Fig. S5(c) in the ESM). Fortunately, the recondensation of Si–OH groups derived from the dissolution of the SiO_2 shell does not occur in the etchant with pH between 1 and 4, as proved by the observations shown in Fig. 5, which shows that there is a big cavity inside the SiO_2 shell and the outer surface of the SiO_2 shell is smooth. However, the Fe_3O_4 core is almost etched away at pH 1 (Fig. 5(a)).

Because the Fe_3O_4 core is acid sensitive, it is important

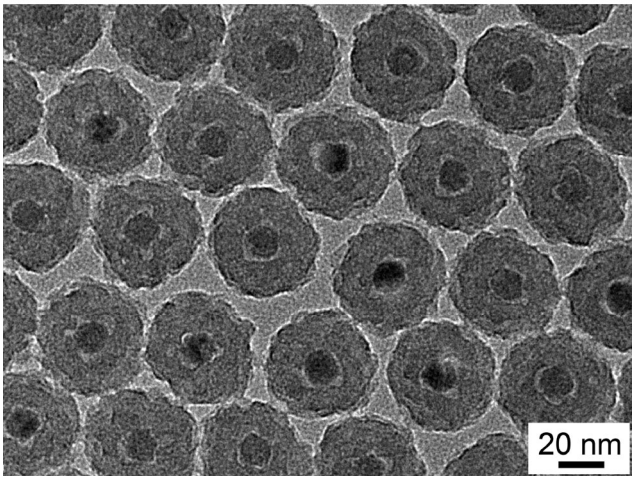

Figure 4 TEM image of yolk/shell Fe_3O_4@SiO_2 NPs after etching in ammonia solution.

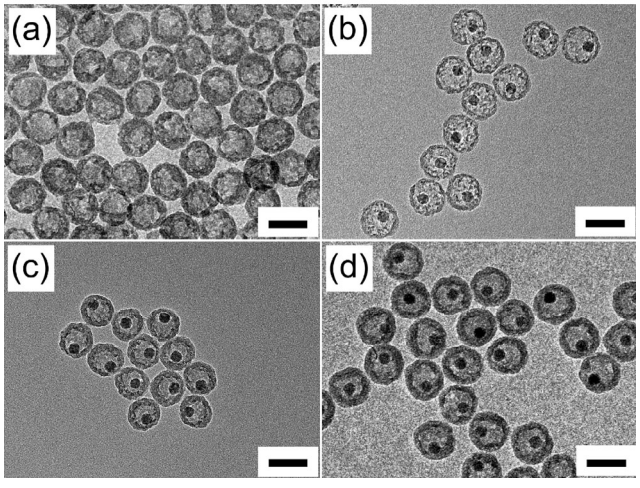

Figure 5 TEM images of yolk/shell Fe_3O_4@SiO_2 NPs with an etchant of pH (a) 1.0, (b) 2.1, (c) 3.2, and (d) 3.6. Scale bar = 50 nm.

to prevent it from erosion during the etching of the SiO_2 shell. Fe_3O_4 is crystalline with relatively strong bonds and its activation energy of dissolution is higher than 10 kcal/mol, and an etchant with pH less than 1 is generally required to dissolve it [48], as demonstrated in Fig. 5(a). In contrast, the SiO_2 shell is an amorphous structure with a low cross-linking degree and has an activation energy of dissolution lower than 5 kcal/mol [49]. Therefore, the breakage of the Fe–O bond is more difficult than the Si–O bond. Nevertheless, it was found that both the Fe_3O_4 core and the SiO_2 shell can be completely dissolved if the etchant pH is below 1. In contrast, the Fe_3O_4 core can be completely preserved and the SiO_2 shell can be entirely dissolved in the etchant with pH values over 2 under the conditions shown in Fig. S6 (in the ESM), because of a low core/shell Fe_3O_4@SiO_2 NP content. Yolk/shell Fe_3O_4@SiO_2 NPs with perfect Fe_3O_4 cores can be formed at pH = 2–4 (Figs. 5(b)–5(d)). No Fe ions were detected from the ICP-MS analysis using the etching parameters described in Figs. 5(b)–5(d) (at ppb level), providing further evidence that the dissolution of the Fe_3O_4 core is more difficult than that of the SiO_2 shell in the etchant with pH 2–4. In contrast, even at pH = 1, if the dissolved SiO_2 soon reaches its saturation state while the dissolved Fe_3O_4 is far from saturation, a hollow SiO_2 structure can be obtained (Fig. 5(a)). In general, the dissolution rate will increase with an increasing undersaturation degree of the oxides [48], and a high undersaturation at pH < 1 will result in the dissolution of Fe_3O_4.

Taking into account the fact that the condensation rate of Si–OH is the minimum at the isoelectric point at pH = 2 [50, 51] and combined with our experimental results (see detailed description in the ESM), the dependence of the recondensation rate of Si–OH groups on the pH value can be schematically illustrated, as shown in Fig. 6. Obviously, the recondensation rate is rather low at pH of 1–4, and increases quickly upon increasing the pH from 4 to 7. According to the above results, it can be concluded that the optimal pH of the etchant should be 2–4 for effectively avoiding the

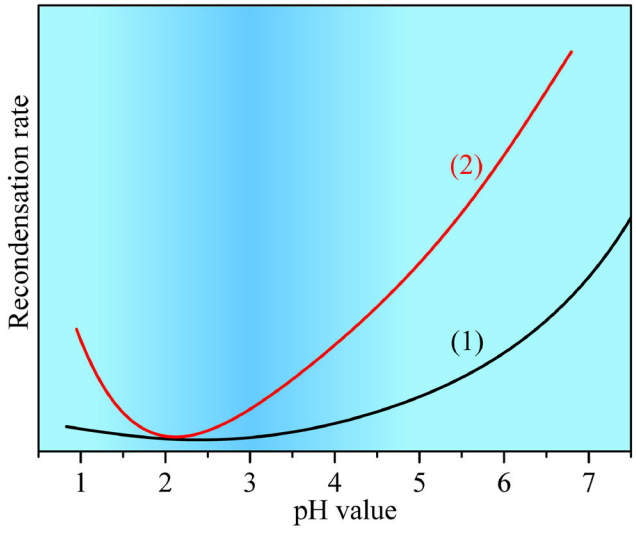

Figure 6 Dependence of the recondensation rate of Si–OH groups of the dissolved silicate species on the etchant pH with two different ionic strengths. Ionic strength increases form curve (1) to curve (2).

reversible condensation of the Si–OH groups on the SiO_2 shell, simultaneously keeping the Fe_3O_4 core intact. As shown in Fig. (6), the recondensation rate of the Si–OH groups will increase rapidly with increasing ionic strength of the etchant [51], accompanied with an enhanced etching rate, resulting in an increased reconstruction rate of the Si–O–Si bond on the SiO_2 shell, which is unfavorable for achieving uniform yolk/shell Fe_3O_4@SiO_2 NPs (Fig. S8(b) in the ESM).

Besides the pH value, factors like the amount of the core/shell Fe_3O_4@SiO_2 NPs, reaction time, and reaction temperature were also investigated to determine the optimal conditions for modulating the cavity and thickness of the SiO_2 shell. The core/shell Fe_3O_4@SiO_2 NPs with a Fe_3O_4 core size of about 13.1 nm was used in these studies. First, the effect of the amount of the core/shell Fe_3O_4@SiO_2 NPs with a shell thickness of 18.1 nm was investigated. It was found that when the amount of the core/shell Fe_3O_4@SiO_2 NPs was only 5 mg, the SiO_2 shell was completely etched off, leaving only the Fe_3O_4 cores (Fig. S9(a) in the ESM). When the amount increased to 8 mg, the SiO_2 shell collapsed completely, and the residual Fe_3O_4 NPs were surrounded by some dissolved silica oligomers (Fig. S9(b) in the ESM). A thin SiO_2 shell with partial openings can be observed when the NP content increased to 12 mg (Fig. S9(c) in the ESM). The retained SiO_2 shell with a perfect structure and a thickness of about 4.4 nm can be obtained when the NP content increased to 14 mg (Fig. 1(d)). Upon further increasing the NP content, the thickness of the retained SiO_2 shell increases gradually, with a well-maintained Fe_3O_4@SiO_2 NPs structure, and when the NPs content increased to 32 mg, the thickness of the SiO_2 shell was 13.0 nm, see Fig. S9(d) in the ESM. ICP-AES analysis was used to determine the Si content from the dissolved SiO_2 in the reaction solution, and the result (Fig. 7) revealed that the Si content gradually increases with increasing core/shell Fe_3O_4@SiO_2 NP content. It reaches the maximum value when the NP content is 16 mg, and then, nearly maintains a constant value upon further increasing the NPs content. This result indicates that there is a maximum solubility of silica in the etchant. When the silica concentration is below the maximum solubility, the SiO_2 shell will be dissolved completely. On the other hand when the silica solubility reaches the maximum value, the dissolution–diffusion equilibrium of silica is well-established, and the SiO_2 shell can be controllably preserved. This kind of equilibrium can be easily achieved with enough Si, and the cavity will be gradually reduced with increasing silica concentration. From Fig. 7, one can see that the Si content has not reached the maximum value when the NP content is 12 mg, but a thin SiO_2 shell is still present, which is considered to be because of the different compactness of the inner and outer part of the SiO_2 shell. The loose inner silica shell has a high solubility and will lead to an increase in the dissolved silica species upon increasing the NP content. Similar results have been obtained for a SiO_2 shell with about 11.1 nm thickness (Fig. S10 in the ESM), indicating that the dissolution–diffusion equilibrium of silica is essential for maintaining an appropriate thickness of the retained SiO_2 shell, as further confirmed by using the ethanol/water mixture as an etching solution (Fig. S11 in the ESM). In the etching solution, the volume ratio of ethanol to water is 1:4, and the cavity volume between the Fe_3O_4 core and the SiO_2 shell decreases substantially compared to that without ethanol because of a low solubility of silica in ethanol [52].

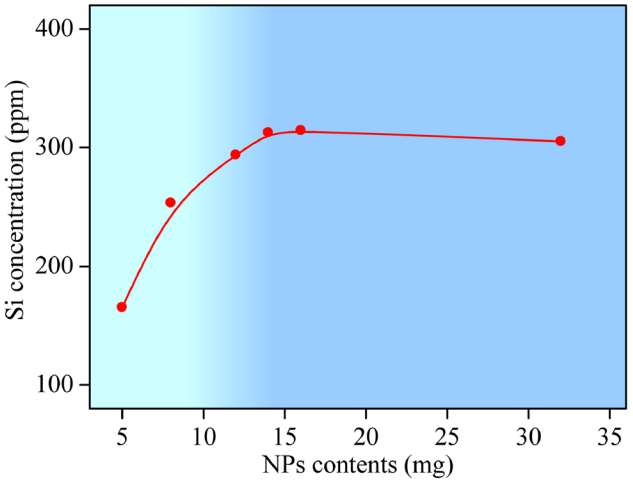

Figure 7 Dependence of the amount of the dissolved silicon species on the core/shell Fe_3O_4@SiO_2 NP content with a shell thickness of 18.1 nm.

The second factor is reaction time. Upon increasing the reaction time from 0 to 24 h, the thickness of the SiO_2 shell gradually decreases from about 18.1 to 8.3 nm (Figs. 1(a) and 1(b)). Upon further increasing the reaction time from 24 h to 48 h, the thickness of

the SiO_2 shell is nearly constant (Fig. S12 in the ESM). ICP-AES analysis (Fig. S13 in the ESM) shows that the Si content of the dissolved SiO_2 in the treated solution increases with increasing reaction time from 0 to 24 h, and then, maintains a nearly constant value upon further increasing the reaction time because of the establishment of the dissolution–diffusion equilibrium for silica at 24 h, and thus, the thickness of the SiO_2 shell remains almost constant.

The reaction temperature is another important factor for the dissolution of the SiO_2 shell. Upon increasing the reaction temperature from 120 to 160 ℃, the thickness of the retained SiO_2 shell gradually decreased (Figs. 8(a), 8(b), and 1(b)), and at 180 ℃, the SiO_2 shell collapsed and is almost completely dissolved, with a few silica oligomers around the Fe_3O_4 NPs (Fig. 8(c)) because of the increased silica solubility at elevated temperatures. ICP-AES analysis (Fig. S14 in the ESM) confirmed that the Si content from the dissolved SiO_2 in the etchant increases with increasing reaction temperature.

During the acidic etching of the SiO_2 shell, the hydrolysis reaction of the silica network undergoes a process similar to nucleophilic substitution [51], as shown in Fig. 9. The Si–O–Si bonds are first protonated, and then, the Si atom is attacked by a water molecule from the back (the transition state in Fig. 9, achieving sp^2 hybridization), as can be proved from the acidic etchant of the PVP-10 aqueous solution. It was found that the PVP-10 aqueous solution of pH 4.6 is also an effective etchant for the SiO_2 shell, as shown in Fig. S15 in the ESM, in which some voids appear between the Fe_3O_4 cores and the SiO_2 shell. As PVP-10 is adsorbed only on the layers near the surface of the SiO_2 shell, the etching of the innermost part of the SiO_2 shell is attributed to the penetration of hydrogen ions from the acidic PVP-10 aqueous solution. This result further demonstrates that the protonation of the Si–O–Si bond by the hydrogen ions is essential for etching the SiO_2 shell. It was found that pure SiO_2 NPs also can be easily converted into hollow SiO_2 nanospheres by using our "standard etching code", as shown in Fig. S16 in the ESM, which provides further evidence that the etching of the SiO_2 shell takes place from the inside to the outside, and is not influenced by the presence of the Fe_3O_4 core. Finally, nucleophilic substitution will take place and the structure of the molecule will be reversed (from sp^2 hybridization to sp^3 hybridization).

From the above discussion, it is clear that the Si atoms attached to the three –OH groups in the innermost part of the SiO_2 shell will be attacked first by water molecules with the aid of hydrogen ions (region I in Fig. 10), because less energy is needed to hydrolyze the Si–O–Si bond when the Si atoms are attached with more –OH groups. On the other hand,

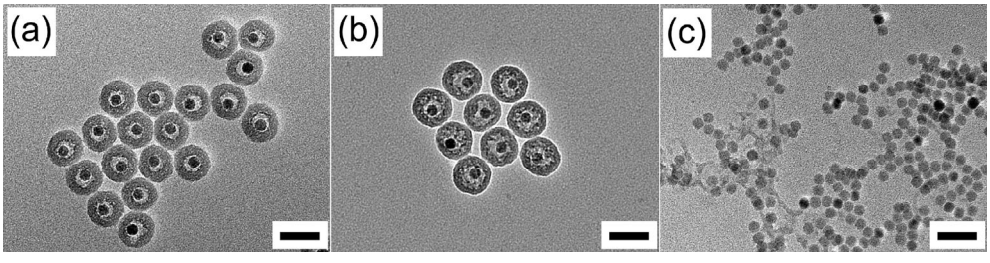

Figure 8 TEM images of yolk/shell Fe_3O_4@SiO_2 NPs etched at (a) 120, (b) 140, and (c) 180 °C. Scale bar = 50 nm.

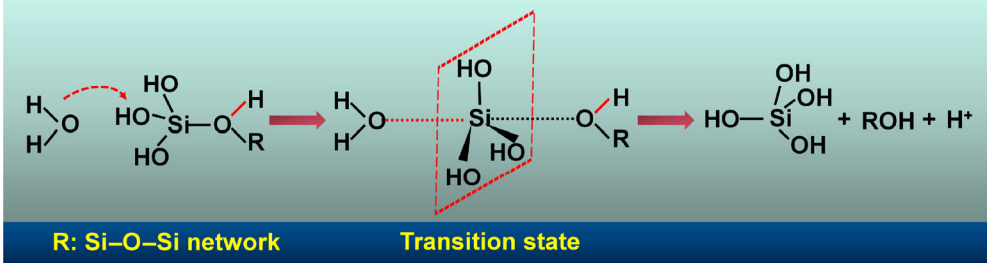

Figure 9 Etching mechanism of SiO_2 shell based on a gentle acidic solution.

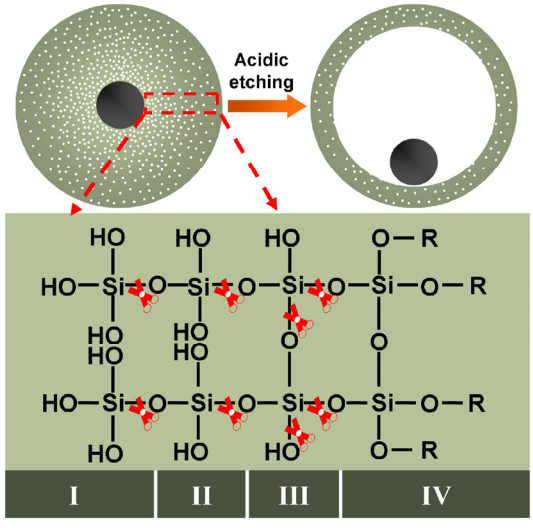

Figure 10 Schematic illustration of acidic etching procedures of the SiO_2 shell. R is the silica network.

the Si atom attached with two –OH groups (region II in Fig. 10) will be hydrolyzed as the Si–O–Si bond in region I was broken. The dissolution rate of the SiO_2 shell will decrease with increasing degree of condensation, as the structural reversal of the long Si–O–Si chain and branches without Si–OH groups will become difficult with a high condensation degree because of the steric hindrance effect, and thus, the etching rate will gradually decrease with the etching reaction, and finally, terminate at the dissolution–diffusion equilibrium of silica. This etching process was confirmed by the correlation between the dissolved Si species content in the reaction solution and the etching time, as shown in Fig. S13 in the ESM, in which the content of the dissolved Si species increases quickly in the initial stage, then increases slightly, and finally, reaches a saturation value, indicating a successful etching process.

Based on above analysis, we can conclude that an increased compactness gradient in the silica shell from the inside to the outside and an appropriate etchant pH value are essential for the preparation of the yolk/shell Fe_3O_4@SiO_2 NPs from the core/shell Fe_3O_4@SiO_2 NPs by selective acidic etching. Since no sacrificial templates and surface protective agents were used during etching, the sub-100 nm yolk/shell Fe_3O_4@SiO_2 NPs have a clean surface, which is beneficial for confined-space catalysis for nanoreactors and bioapplications for nanomedicines.

The magnetic properties of core/shell and yolk/shell Fe_3O_4@SiO_2 NPs were investigated, and the result is shown in Fig. S17 (in the ESM). It was found that the saturation magnetization increases remarkably after acidic etching, from 2.8 emu/g for the core/shell to 9.8 emu/g for the yolk/shell Fe_3O_4@SiO_2 NPs. Nevertheless, when normalized to the Fe_3O_4 content, the corresponding saturation magnetization is 52.8 and 48.4 emu/g, respectively, which can be regarded as nearly the same. This result proved that the acidic etching has almost no influence on the magnetic property of Fe_3O_4 NPs. In reality, the superparamagnetic characteristics and high saturation magnetization of the yolk/shell Fe_3O_4@SiO_2 NPs is beneficial for applications such as magnetically targeted drug delivery vehicles and magnetic resonance contrast.

4 Conclusions

In summary, we have developed a mild acidic etching method based on a silica self-template for the preparation of yolk/shell Fe_3O_4@SiO_2 NPs with sizes less than 100 nm. The acid-sensitive Fe_3O_4 core can be perfectly preserved and the SiO_2 shell can be selectively etched away. The etching starts from the inside to the outside of the SiO_2 shell because of the gradually increasing degree of compactness of the SiO_2 shell. We found that silica etching in etchants like HCl and CH_3COOH is irreversible at pH 1–4, which provides an excellent strategy for silica etching chemistry. The cavity and thickness of the SiO_2 shell can be regulated simply by the amount of the core/shell Fe_3O_4@SiO_2 NPs, reaction time, and reaction temperature. The sub-100 nm yolk/shell Fe_3O_4@SiO_2 NPs with controlled shell thickness and cavity can have potential applications in biomedical fields. Our method can be extended to other yolk/shell functional core/silica nanostructures for various applications.

Acknowledgements

The authors gratefully acknowledge the financial support from the National Natural Science Foundation of China (Nos. 51502298 and 51572263), National Basic Research Program of China (No. 2013CB934304)

and the China Postdoctoral Science Foundation (No. 2014M561844).

Electronic Supplementary Material: Supplementary material (further details of TEM images, ICP-AES results, nitrogen adsorption–desorption isotherm, Tables S1 and S2) is available in the online version of this article at http://dx.doi.org/10.1007/s12274-016-1233-4.

References

[1] Priebe, M.; Fromm, K. M. Nanorattles or yolk–shell nanoparticles—What are they, how are they made, and what are they good for? *Chem. —Eur. J.* **2015**, *21*, 3854–3874.

[2] Yang, Y.; Liu, X.; Li, X. B.; Zhao, J.; Bai, S. Y.; Liu, J.; Yang, Q. H. A yolk–shell nanoreactor with a basic core and an acidic shell for cascade reactions. *Angew. Chem., Int. Ed.* **2012**, *51*, 9164–9168.

[3] Liu, J.; Qiao, S. Z.; Chen, J. S.; Lou, X. W. D.; Xing, X. R.; Lu, G. Q. M. Yolk/shell nanoparticles: New platforms for nanoreactors, drug delivery and lithium-ion batteries. *Chem. Commun.* **2011**, *47*, 12578–12591.

[4] Li, W.; Deng, Y. H.; Wu, Z. X.; Qian, X. F.; Yang, J. P.; Wang, Y.; Gu, D.; Zhang, F.; Tu, B.; Zhao, D. Y. Hydrothermal etching assisted crystallization: A facile route to functional yolk–shell titanate microspheres with ultrathin nanosheets-assembled double shells. *J. Am. Chem. Soc.* **2011**, *133*, 15830–15833.

[5] Lee, I.; Joo, J. B.; Yin, Y. D.; Zaera, F. A yolk@shell nanoarchitecture for Au/TiO_2 catalysts. *Angew. Chem., Int. Ed.* **2011**, *50*, 10208–10211.

[6] Lv, R. C.; Yang, P. P.; He, F.; Gai, S. L.; Li, C. X.; Dai, Y. L.; Yang, G. X.; Lin, J. A yolk-like multifunctional platform for multimodal imaging and synergistic therapy triggered by a single near-infrared light. *ACS Nano* **2015**, *9*, 1630–1647.

[7] Lu, S.; Tu, D. T.; Hu, P.; Xu, J.; Li, R. F.; Wang, M.; Chen, Z.; Huang, M. D.; Chen, X. Y. Multifunctional nano-bioprobes based on rattle-structured upconverting luminescent nanoparticles. *Angew. Chem., Int. Ed.* **2015**, *54*, 7915–7919.

[8] Fan, W. P.; Shen, B.; Bu, W. B.; Chen, F.; Zhao, K. L.; Zhang, S. J.; Zhou, L. P.; Peng, W. J.; Xiao, Q. F.; Xing, H. Y. et al. Rattle-structured multifunctional nanotheranostics for synergetic chemo-/radiotherapy and simultaneous magnetic/luminescent dual-mode imaging. *J. Am. Chem. Soc.* **2013**, *135*, 6494–6503.

[9] Kang, X. J.; Cheng, Z. Y.; Yang, D. M.; Ma, P. A.; Shang, M. M.; Peng, C.; Dai, Y. L.; Lin, J. Design and synthesis of multifunctional drug carriers based on luminescent rattle-type mesoporous silica microspheres with a thermosensitive hydrogel as a controlled switch. *Adv. Funct. Mater.* **2012**, *22*, 1470–1481.

[10] Kim, J. G.; Kim, S. M.; Lee, I. S. Mechanistic insight into the yolk@shell transformation of MnO@silica nanospheres incorporating Ni^{2+} ions toward a colloidal hollow nanoreactor. *Small* **2015**, *11*, 1930–1938.

[11] Lee, J.; Kim, S. M.; Lee, I. S. Functionalization of hollow nanoparticles for nanoreactor applications. *Nano Today* **2014**, *9*, 631–667.

[12] Fang, X. L.; Liu, Z. H.; Hsieh, M. F.; Chen, M.; Liu, P. X.; Chen, C.; Zheng, N. F. Hollow mesoporous aluminosilica spheres with perpendicular pore channels as catalytic nanoreactors. *ACS Nano* **2012**, *6*, 4434–4444.

[13] Lee, J.; Park, J. C.; Song, H. A nanoreactor framework of a Au@SiO_2 yolk/shell structure for catalytic reduction of p-nitrophenol. *Adv. Mater.* **2008**, *20*, 1523–1528.

[14] Seh, Z. W.; Li, W. Y.; Cha, J. J.; Zheng, G. Y.; Yang, Y.; McDowell, M. T.; Hsu, P.-C.; Cui, Y. Fsulphur-TiO_2 yolk–shell nanoarchitecture with internal void space for long-cycle lithium-sulphur batteries. *Nat. Commun.* **2013**, *4*, 1331.

[15] Hong, Y. J.; Son, M. Y.; Kang, Y. C. One-pot facile synthesis of double-shelled SnO_2 yolk–shell-structured powders by continuous process as anode materials for Li-ion batteries. *Adv. Mater.* **2013**, *25*, 2279–2283.

[16] Liu, N.; Wu, H.; McDowell, M. T.; Yao, Y.; Wang, C. M.; Cui, Y. A yolk–shell design for stabilized and scalable Li-ion battery alloy anodes. *Nano Lett.* **2012**, *12*, 3315–3321.

[17] Chen, Y.; Chen, H. R.; Shi, J. L. Construction of homogenous/heterogeneous hollow mesoporous silica nanostructures by silica-etching chemistry: Principles, synthesis, and applications. *Acc. Chem. Res.* **2014**, *47*, 125–137.

[18] Pérez-Lorenzo, M.; Vaz, B.; Salgueiriño, V.; Correa-Duarte, M. A. Hollow-shelled nanoreactors endowed with high catalytic activity. *Chem.—Eur. J.* **2013**, *19*, 12196–12211.

[19] Gai, S. L.; Yang, P. P.; Li, C. X.; Wang, W. X.; Dai, Y. L.; Niu, N.; Lin, J. Synthesis of magnetic, up-conversion luminescent, and mesoporous core–shell-structured nanocomposites as drug carriers. *Adv. Funct. Mater.* **2010**, *20*, 1166–1172.

[20] Tang, F. Q.; Li, L. L.; Chen, D. Mesoporous silica nanoparticles: Synthesis, biocompatibility and drug delivery. *Adv. Mater.* **2012**, *24*, 1504–1534.

[21] Dong, R. H.; Liu, W. M.; Hao, J. C. Soft vesicles in the synthesis of hard materials. *Acc. Chem. Res.* **2012**, *45*, 504–513.

[22] Zhu, Y. F.; Kockrick, E.; Ikoma, T.; Hanagata, N.; Kaskel, S. An efficient route to rattle-type Fe_3O_4@SiO_2 hollow mesoporous spheres using colloidal carbon spheres templates. *Chem. Mater.* **2009**, *21*, 2547–2553.

[23] Caruso, F.; Caruso, R. A.; Möhwald, H. Nanoengineering of inorganic and hybrid hollow spheres by colloidal templating. *Science* **1998**, *282*, 1111–1114.

[24] Yang, Y.; Liu, J.; Li, X. B.; Liu, X.; Yang, Q. H. Organosilane-assisted transformation from core–shell to yolk–shell nanocomposites. *Chem. Mater.* **2011**, *23*, 3676–3684.

[25] Liu, J.; Qiao, S. Z.; Hartono, S. B.; Lu, G. Q. Monodisperse yolk–shell nanoparticles with a hierarchical porous structure for delivery vehicles and nanoreactors. *Angew. Chem., Int. Ed.* **2010**, *49*, 4981–4985.

[26] Wu, X. J.; Xu, D. S. Formation of yolk/SiO_2 shell structures using surfactant mixtures as template. *J. Am. Chem. Soc.* **2009**, *131*, 2774–2775.

[27] Chen, Y.; Chen, H. R.; Guo, L. M.; He, Q. J.; Chen, F.; Zhou, J.; Feng, J. W.; Shi, J. L. Hollow/rattle-type mesoporous nanostructures by a structural difference-based selective etching strategy. *ACS Nano* **2010**, *4*, 529–539.

[28] Chen, D.; Li, L. L.; Tang, F. Q.; Qi, S. Facile and scalable synthesis of tailored silica "nanorattle" structures. *Adv. Mater.* **2009**, *21*, 3804–3807.

[29] Zhang, Q.; Zhang, T. R.; Ge, J. P.; Yin, Y. D. Permeable silica shell through surface-protected etching. *Nano Lett.* **2008**, *8*, 2867–2871.

[30] Zhang, Q.; Ge, J. P.; Goebl, J.; Hu, Y. X.; Lu, Z. D.; Yin, Y. D. Rattle-type silica colloidal particles prepared by a surface-protected etching process. *Nano Res.* **2009**, *2*, 583–591.

[31] Colombo, M.; Carregal-Romero, S.; Casula, M. F.; Gutiérrez, L.; Morales, M. P.; Böhm, I. B.; Heverhagen, J. T.; Prosperi, D.; Parak, W. J. Biological applications of magnetic nanoparticles. *Chem. Soc. Rev.* **2012**, *41*, 4306–4334.

[32] Purbia, R.; Paria, S. Yolk/shell nanoparticles: Classifications, synthesis, properties, and applications. *Nanoscale* **2015**, *7*, 19789–19873.

[33] Zhang, L. Y.; Wang, T. T.; Yang, L.; Liu, C.; Wang, C. G.; Liu, H. Y.; Wang, Y. A.; Su, Z. M. General route to multifunctional uniform yolk/mesoporous silica shell nanocapsules: A platform for simultaneous cancer-targeted imaging and magnetically guided drug delivery. *Chem.—Eur. J.* **2012**, *18*, 12512–12521.

[34] Hu, Y. X.; Zhang, Q.; Goebl, J.; Zhang, T. R.; Yin, Y. D. Control over the permeation of silica nanoshells by surface-protected etching with water. *Phys. Chem. Chem. Phys.* **2010**, *12*, 11836–11842.

[35] Park, S. J.; Kim, Y. J.; Park, S. J. Size-dependent shape evolution of silica nanoparticles into hollow structures. *Langmuir* **2008**, *24*, 12134–12137.

[36] Song, X. H.; Ding, T.; Yao, L.; Lin, M.; Tan, R. L. S.; Liu, C. C.; Sokol, K.; Yu, L.; Lou, X. W.; Chen, H. Y. On the origin and underappreciated effects of ion doping in silica. *Small* **2015**, *11*, 4351–4365.

[37] Yu, Q. Y.; Wang, P. P.; Hu, S.; Hui, J. F.; Zhuang, J.; Wang, X. Hydrothermal synthesis of hollow silica spheres under acidic conditions. *Langmuir* **2011**, *27*, 7185–7191.

[38] Kim, J.; Kim, H. S.; Lee, N.; Kim, T.; Kim, H.; Yu, T.; Song, I. C.; Moon, W. K.; Hyeon, T. Multifunctional uniform nanoparticles composed of a magnetite nanocrystal core and a mesoporous silica shell for magnetic resonance and fluorescence imaging and for drug delivery. *Angew. Chem., Int. Ed.* **2008**, *47*, 8438–8441.

[39] Yi, D. K.; Lee, S. S.; Papaefthymiou, G. C.; Ying, J. Y. Nanoparticle architectures templated by SiO_2/Fe_2O_3 nanocomposites. *Chem. Mater.* **2006**, *18*, 614–619.

[40] Park, J.; An, K. J.; Hwang, Y.; Park, J. G.; Noh, H. J.; Kim, J. Y.; Park, J. H.; Hwang, N. M.; Hyeon, T. Ultra-large-scale syntheses of monodisperse nanocrystals. *Nat. Mater.* **2004**, *3*, 891–895.

[41] Ding, H. L.; Zhang, Y. X.; Wang, S.; Xu, J. M.; Xu, S. C.; Li, G. H. Fe_3O_4@SiO_2 core/shell nanoparticles: The silica coating regulations with a single core for different core sizes and shell thicknesses. *Chem. Mater.* **2012**, *24*, 4572–4580.

[42] Osseo-Asare, K.; Arriagada, F. J. Growth kinetics of nanosize silica in a nonionic water-in-oil microemulsion: A reverse micellar pseudophase reaction model. *J. Colloid Interface Sci.* **1999**, *218*, 68–76.

[43] Alexander, G. B. The effect of particle size on the solubility of amorphous silica in water. *J. Phys. Chem.* **1957**, *61*, 1563–1564.

[44] Chen, S. L.; Dong, P.; Yang, G. H.; Yang, J. J. Kinetics of formation of monodisperse colloidal silica particles through the hydrolysis and condensation of tetraethylorthosilicate. *Ind. Eng. Chem. Res.* **1996**, *35*, 4487–4493.

[45] Wong, Y. J.; Zhu, L. F.; Teo, W. S.; Tan, Y. W.; Yang, Y. H.; Wang, C.; Chen, H. Y. Revisiting the stöber method: Inhomogeneity in silica shells. *J. Am. Chem. Soc.* **2011**, *133*, 11422–11425.

[46] Liu, J. N.; Bu, J. W.; Bu, W. B.; Zhang, S. J.; Pan, L. M.; Fan, W. P.; Chen, F.; Zhou, L. P.; Peng, W. J.; Zhao, K. L. et al. Real-time *in vivo* quantitative monitoring of drug release by dual-mode magnetic resonance and upconverted luminescence imaging. *Angew. Chem., Int. Ed.* **2014**, *53*, 4551–4555.

[47] Zhao, L.; Zhao, Y. F.; Han, Y. Pore fabrication in various silica-based nanoparticles by controlled etching. *Langmuir* **2010**, *26*, 11784–11789.

[48] Cornell, R. M.; Schwertmann, U. *The Iron Oxides: Structure, Properties, Reactions, Occurrences and Uses, Seconded*, 2nd ed.; Wiley-VCH: Weinheim, 2003.

[49] Greenberg, S. A. Thermodynamic functions for the solution of silica in water. *J. Phys. Chem.* **1957**, *61*, 196–197.

[50] Wu, S. H.; Mou, C. Y.; Lin, H. P. Synthesis of mesoporous silica nanoparticles. *Chem. Soc. Rev.* **2013**, *42*, 3862–3875.

[51] Ghosh Chaudhuri, R.; Paria, S. Core/shell nanoparticles: Classes, properties, synthesis mechanisms, characterization, and applications. *Chem. Rev.* **2012**, *112*, 2373–2433.

[52] Bogush, G. H.; Zukoski, C. F. Studies of the kinetics of the precipitation of uniform silica particles through the hydrolysis and condensation of silicon alkoxides. *J. Colloid Interface Sci.* **1991**, *142*, 1–18.